The Astrophysical Journal, 661:102–114, 2007 May 20

DUST AND ATOMIC GAS IN DWARF IRREGULAR GALAXIES OF THE M81 GROUP: THE SINGS AND THINGS VIEW

Fabian Walter,[1] John M. Cannon,[1,2] Hélène Roussel,[1] George J. Bendo,[3] Daniela Calzetti,[4] Daniel A. Dale,[5] Bruce T. Draine,[6] George Helou,[7] Robert C. Kennicutt, Jr.,[8,9] John Moustakas,[9,10] George H. Rieke,[9] Lee Armus,[7] Charles W. Engelbracht,[9] Karl Gordon,[9] David J. Hollenbach,[11] Janice Lee,[9] Aigen Li,[12] Martin J. Meyer,[4] Eric J. Murphy,[13] Michael W. Regan,[4] John-David T. Smith,[9] Elias Brinks,[14] W. J. G. de Blok,[15] Frank Bigiel,[1] and Michele D. Thornley[16]

Received 2006 September 26; accepted 2007 February 12

ABSTRACT

We present observations of the dust and atomic gas phase in seven dwarf irregular galaxies of the M81 group from the *Spitzer* SINGS and VLA THINGS surveys. The *Spitzer* observations provide a first glimpse of the nature of the nonatomic ISM in these metal-poor ($Z \sim 0.1\ Z_\odot$), quiescent (SFR ~ 0.001–$0.1\ M_\odot\ \mathrm{yr}^{-1}$) dwarf galaxies. Most detected dust emission is restricted to H I column densities $>1 \times 10^{21}\ \mathrm{cm}^{-2}$, and almost all regions of high H I column density ($>2.5 \times 10^{21}\ \mathrm{cm}^{-2}$) have associated dust emission. *Spitzer* spectroscopy of two regions in the brightest galaxies (IC 2574 and Holmberg II) show distinctly different spectral shapes and aromatic features, although the galaxies have comparable gas-phase metallicities. This result emphasizes that the strength of the aromatic features is not a simple linear function of metallicity. We estimate dust masses of $\sim 10^4$–$10^6\ M_\odot$ for the M81 dwarf galaxies, resulting in an average dust-to-gas ratio ($M_{\mathrm{dust}}/M_{\mathrm{H\,I}}$) of $\sim 3 \times 10^{-4}$ (1.5×10^{-3} if only the H I that is associated with dust emission is considered); this is an order of magnitude lower than the typical value derived for the SINGS spirals. The dwarf galaxies are underluminous per unit star formation rate at 70 μm as compared to the more massive galaxies in SINGS by a factor of ~ 2. However, the average 70/160 μm ratio in the sample dwarf galaxies is higher than what is found in the other galaxies of the SINGS sample. This can be explained by a combination of a lower dust content in conjunction with a higher dust temperature in the dwarfs.

Subject headings: galaxies: dwarf — galaxies: individual (DDO 53, DDO 165, Holmberg I, Holmberg II, IC 2574, M81 dwA, M81 dwB) — galaxies: irregular — galaxies: ISM — infrared: galaxies

1. INTRODUCTION

Nearby dwarf galaxies have proven to be ideal laboratories to investigate how stars form out of gas and how, in turn, violent star formation shapes the ambient interstellar medium (ISM). These systems are highly susceptible to the formation of shells and holes in the neutral gas phase; more energetic star formation can lead to the formation of gaseous outflows from these systems. Previous studies have shown that dwarf galaxies can be used as test beds of "simple" prescriptions for star formation (since these systems are typically in solid-body rotation and are therefore less affected by shear in the ISM) and for understanding the connection between mechanical energy input into the ISM ("feedback") and future star formation. Given their low metallicities, they also provide a unique opportunity to study the conditions of the ISM in environments that may resemble those in the earliest star-forming systems at high redshift.

Based on their ISM properties, dwarf galaxies can be roughly divided into two subgroups: gas-rich dwarf irregulars (dIrrs) and gas-poor dwarf spheroidals/ellipticals (dSph/dE). The gas-rich dIrrs are particularly interesting for studies of current star formation, since they still contain the "fuel" for star formation. Although many studies have shown that these objects are rich in atomic hydrogen (H I; for a review see Skillman 1996), little is known about their molecular gas properties. Many searches for molecular gas (through observations of the most abundant tracer molecule, CO) have been performed but very few dwarf galaxies have been detected in CO so far: no dwarf has been detected in CO at metallicities $\lesssim 10\%\ Z_\odot$ (Taylor et al. 1998; Barone et al. 2000; Leroy et al. 2005).

Similarly, little is known about the dust properties in faint, low-metallicity dwarf galaxies. Some of the brightest dwarfs have been detected with previous far-infrared (far-IR) observatories such as *IRAS* and *ISO* (see, e.g., Hunter et al. 1989; Gallagher et al. 1991; Melisse & Israel 1994a, 1994b; Hunter et al. 2001). These early studies found that dwarfs typically have higher dust temperatures than those derived for more massive galaxies, with the peak of the infrared spectral energy distribution (SED) shifted to shorter wavelengths.

The more typical "quiescent" dIrr galaxies (with SFR $\leq 0.1\ M_\odot\ \mathrm{yr}^{-1}$) had remained undetected in the far-IR prior to the advent of the *Spitzer Space Telescope*; its dramatically increased sensitivity compared to previous observatories has opened up the

[1] Max-Planck-Institut für Astronomie, D-69117 Heidelberg, Germany.
[2] Astronomy Department, Wesleyan University, Middletown, CT 06459.
[3] Imperial College London, London SW7 2AZ, UK.
[4] Space Telescope Science Institute, Baltimore, MD 21218.
[5] Department of Physics and Astronomy, University of Wyoming, Laramie, WY 82071.
[6] Princeton University Observatory, Princeton, NJ 08544.
[7] California Institute of Technology, Pasadena, CA 91101.
[8] Institute of Astronomy, University of Cambridge, Cambridge CB3 0HA, UK.
[9] Steward Observatory, University of Arizona, Tucson, AZ 85721.
[10] Department of Physics, New York University, New York, NY 10003.
[11] NASA/Ames Research Center, Moffett Field, CA, 94035.
[12] Department of Physics and Astronomy, University of Missouri, Columbia, MO 65211.
[13] Department of Astronomy, Yale University, New Haven, CT 06520.
[14] Centre for Astrophysics Research, University of Hertfordshire, Hatfield AL10 9AB, UK.
[15] Research School of Astronomy & Astrophysics, Mount Stromlo Observatory, Weston ACT 2611, Australia.
[16] Department of Physics, Bucknell University, Lewisburg, PA 17837.

TABLE 1
PROPERTIES OF THE SAMPLE DWARF GALAXIES IN THE M81 GROUP

Galaxy	D[a] (Mpc)	$F_{\rm H\,I}$ (Jy km s^{-1})	$M_{\rm H\,I}$ ($10^8\ M_\odot$)	$\log F({\rm H}\alpha)$[b] (ergs s^{-1} cm^{-2})	$12 + \log({\rm O/H})$[c]	$S(24\ \mu{\rm m})$[d] (Jy)	$S(70\ \mu{\rm m})$[d] (Jy)	$S(160\ \mu{\rm m})$[d] (Jy)
IC 2574	4.02	386.7	14.75	−11.27	7.94 ± 0.06	0.28 ± 0.013	5.55 ± 0.42	11.75 ± 1.50
Holmberg II	3.39	219.3	5.95	−11.30	7.68 ± 0.03	0.20 ± 0.008	3.67 ± 0.26	4.46 ± 0.58
Holmberg I	3.84	40.1	1.40	−12.43	7.54 ± 0.34	0.013 ± 0.002	0.41 ± 0.08	0.90 ± 0.17
DDO 165	4.57	35.0	1.72	−12.93	7.76 ± 0.18[e]	<0.014	<0.15	<0.33
DDO 053	3.56	20.0	0.60	−12.24	7.77 ± 0.1	0.029 ± 0.001	0.40 ± 0.03	0.50 ± 0.11
M81 DwB	5.3	3.8	0.25	−12.82	7.85 ± 0.17	0.009 ± 0.001	0.15 ± 0.03	0.39 ± 0.18
M81 DwA	3.55	4.1	0.12	...	...	<0.002	<0.17	<0.15

[a] Distances are from Karachentsev et al. (2002, 2003).
[b] Hα fluxes are from R. Kennicutt et al. (2007, in preparation) and Lee (2006).
[c] Characteristic gas phase oxygen abundances from J. Moustakas et al. (2007, in preparation), based on the Pilyugin & Thuan (2005) strong-line calibration of $R_{23} = ([{\rm O\,II}] + [{\rm O\,II}])/{\rm H}\beta$; $12 + \log({\rm O/H})_\odot = 8.7$ (Asplund et al. 2005).
[d] Flux densities adopted from Dale et al. (2006).
[e] Based on the luminosity-metallicity relation, J. Moustakas et al. (2007, in preparation).

low-metallicity regime of the extragalactic ISM to exploration in the far-IR. Early *Spitzer* observations have naturally concentrated on the brightest and most extremely metal-poor dwarfs. Houck et al. (2004b) show that SBS 0335−052, one of the most metal-poor dwarf galaxies known, has an exceptional SED that is shifted blueward with a peak at ∼28 μm (compared to ∼80 μm for more metal-rich starburst galaxies and >100 μm for local star-forming spirals). Engelbracht et al. (2004) presented observations of the dwarf galaxy NGC 55, and a larger sample of galaxies showed that there is a metallicity threshold above which emission from aromatic features appear (Engelbracht et al. 2005). Smith et al. (2007) used *Spitzer* spectroscopy to study how the spectral signatures of aromatic features change as a function of metallicity. Other recent *Spitzer* studies of actively star-forming dwarf galaxies include spectroscopic observations by Wu et al. (2006) and O'Halloren et al. (2006), and imaging studies of star-forming dwarfs and Local Group galaxies (including dwarf galaxies) by Rosenberg et al. (2006) and Jackson et al. (2006). Cannon et al. (2005, 2006a, 2006b) have presented detailed *Spitzer* studies of some of the most luminous and nearby dwarfs (IC 2574, NGC 1705, and NGC 6822). These case studies have shown that localized star formation has dramatic effects on the multiphase ISM, altering the relative strengths of nebular, far-IR dust, and radio continuum emission.

Here we discuss the distribution of dust and atomic hydrogen in seven dwarf irregular galaxies in the M81 group of galaxies. Our sample spans 2 orders of magnitude in H I masses and a similar range in star formation rates, from $<0.001\ M_\odot\ {\rm yr}^{-1}$ (Hα nondetections) to $\sim 0.1\ M_\odot\ {\rm yr}^{-1}$. The general properties of the sample dwarfs are summarized in Table 1. All these dwarf irregular galaxies are part of the *Spitzer* Infrared Nearby Galaxies Survey (SINGS; see Kennicutt et al. 2003) and have also been included in The H I Nearby Galaxy Survey (THINGS; Walter et al. 2005).

This paper is organized as follows. In § 2 we summarize the *Spitzer* MIPS and the VLA H I observations. In § 3 we present our results, i.e., the distribution of the atomic gas and the dust, IRS spectra of two galaxies, estimates of the dust masses, and a comparison to other galaxies in the SINGS sample. In § 4 we present a summary of our study.

2. OBSERVATIONS

2.1. *Spitzer* MIPS Observations

The 24, 70, and 160 μm data were taken with MIPS on the *Spitzer Space Telescope* as part of the SINGS survey (Kennicutt et al. 2003). The observations were obtained using the scan-mapping mode in two separate visits to each galaxy (facilitating removal of asteroids and detector artifacts). Each pixel in the map was observed 40, 20, and 4 times at 24, 70, and 160 μm, respectively, resulting in integration times per pixel of 160, 80, and 16 s, respectively. All MIPS data were processed using the MIPS Instrument Team Data Analysis Tool (Gordon et al. 2005). Systematic uncertainties (e.g., detector nonlinearities, time-dependent responsivity variations, background removal, etc.) limit the absolute flux calibration to ∼4%, 7%, and 12% in the MIPS 24, 70, and 160 μm bands. The FWHM of the MIPS point-spread functions (PSFs) are 6″, 18″, and 40″ at 24, 70, and 160 μm, respectively. For more details on the MIPS data reduction, see Bendo et al. (2006); for a general description of the SINGS observing strategies, see Kennicutt et al. (2003).

The flux densities presented in this paper were derived for apertures much larger than the MIPS PSFs, and therefore aperture corrections have not been applied. The M81 group is located in a direction in which the Galaxy is rich in infrared cirrus (de Vries et al. 1987). Inspection of individual images reveals that Galactic cirrus emission is indeed present in the longer wavelength MIPS images. However, this emission is distributed over much larger angular scales than the sources of interest and can thus be easily separated from the galaxies presented in this study.

The aperture for each individual galaxy has been chosen carefully to encompass all the emission visible in all three MIPS bands; apertures were compared with IRAC band 1 and H I imaging to ensure that the total galaxy extent (i.e., gas and stars) was measured. For each individual galaxy, we used the same aperture to extract the flux densities from the three MIPS bands. To account for the variations in the background (both instrumental and due to Galactic cirrus) we have defined multiple background regions for each galaxy that contain the same area as the target aperture. The (background-subtracted) source flux densities we derived using this technique are the same (within the errors) as the values derived by Dale et al. (2005, 2006) in their study of the entire SINGS sample. For consistency we therefore adopt the values of Dale et al. (2006) for our study. The global flux densities are summarized in Table 1—note that M81 dwA and DDO 165 are MIPS nondetections. The reader is referred to Dale et al. (2006) for the IRAC flux densities of the dwarf galaxies in our sample.

2.2. *VLA Observations*

H I data for six of the seven M81 group dwarfs presented here were obtained as part of THINGS, a survey to obtain high-resolution

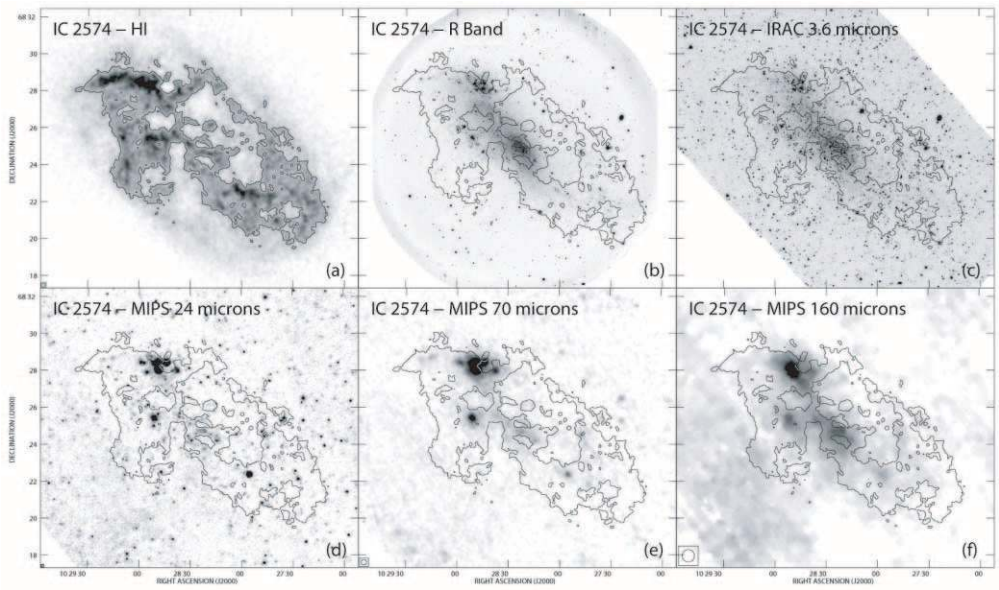

FIG. 1.—IC 2574: (*a*) integrated THINGS H I map (contour shown at $N_{\rm H\,I} = 10^{21}$ cm^{-2} in all panels); (*b*) *R*-band image; (*c*) IRAC 3.6 μm image; (*d*, *e*, and *f*) 24, 70, and 160 μm images, respectively. The sizes of the H I and MIPS beams are given in the lower left corners of their respective panels.

NRAO[17] VLA H I imaging for 35 nearby galaxies (Walter et al. 2005). H I data for DDO 165 were taken from J. M. Cannon et al. 2007 (in preparation).

For THINGS, each galaxy was observed with the *VLA* in D, C, and B configurations with typical integration times of 1.5, 2.5, and 7 hr, respectively. The calibration and data reduction were done using the AIPS package.[18] The absolute flux scale for the data was determined by observing the quasar 3C 286 in all observing runs. The time-variable phase and amplitude calibration were done using the nearby, secondary calibrators 1313+549 and 1252+565, which are unresolved for the arrays used. The *uv* data were inspected for each array and bad data points due to either interference or cross-talk between antennae were removed, after which the data were calibrated. After final editing, all data for each target were combined to form a single data set that was subsequently used to create maps of the brightness distribution on the sky as a function of frequency/velocity (data cubes).

In order to remove the continuum from the line data, we first determined the line-free channels in our observations and subtracted the continuum emission in the (*u, v*)-plane. After that, data cubes (1024 × 1024 pixels × 80 channels each) were produced using the task `imagr` in AIPS. To boost the angular resolution while still maintaining a reasonable noise, we use a `robust` parameter of 0.5 for the final imaging. To ensure that we reach identical beam sizes for all THINGS observations, the data were subsequently convolved to a common resolution of 10″. This resulted in a typical rms noise per channel of 0.5 mJy beam^{-1} for a 2.5 km s^{-1} channel (corresponding to $N_{\rm H\,I} = 1.5 \times 10^{19}$ cm^{-2}). To separate real emission from noise in the final integrated H I maps, we only consider regions that show emission in consecutive channels above a set level ($\sim$2 σ) in slightly convolved (20″) cubes. Note that the data for DDO 165 are at a resolution of 21″.

The fluxes in the integrated THINGS H I map are corrected for the fact that typically the residual flux of the source in cleaned channel maps is overestimated (sometimes by a factor of a few) due to the different beam sizes of the dirty and cleaned beams (for details see, e.g., Jörsäter & van Moorsel 1995; Walter & Brinks 1999). In the integrated H I maps this typically leads to flux corrections of order 25%–40%. To correct for this, we have scaled the residual fluxes by the ratio of the dirty and clean beam sizes and estimate that our column densities are correct within 10% (including the intrinsic uncertainties of the flux calibration; the inferred H I masses are given in Table 1).

3. DUST AND H I CHARACTERISTICS

In Figures 1–7 we present images of the individual galaxies (in order of decreasing H I mass). For each galaxy, we show six panels: panel *a* is the integrated THINGS H I map at 10″ resolution (only exception: DDO 165 beam size: 21″); unless otherwise stated, one H I contour is drawn at $N_{\rm H\,I} = 1 \times 10^{21}$ cm^{-2} (i.e., close to the canonical star formation threshold; e.g., Skillman 1996). An optical *R*-band and the *Spitzer* IRAC band 1 (3.6 μm) image of the galaxies are shown in panels *b* and *c* (the optical images have been observed either at the Calar Alto 2.2 m telescope or are taken from the ancillary SINGS data archive). Panels *d*, *e*, and *f* are the MIPS 24, 70, and 160 μm images of the same area. All panels show the same H I contour as presented in the first panel. The beam sizes for both the H I and MIPS images are shown in the lower left of the respective images.

For each galaxy with THINGS H I imaging, we compare the radial profiles of the H I, 70 and 160 μm MIPS images in Figure 8 (as discussed for the individual systems below). The deprojection parameters (inclination, position angle) used for the creation of the radial profiles have been derived from the H I maps (see caption Fig. 8).

In the following, we briefly discuss the individual galaxies:

IC 2574 (*Fig. 1*).—IC 2574 is the largest galaxy in our sample, and its H I morphology is dominated by the presence of H I holes (Walter & Brinks 1999). The brightest region in the MIPS bands is the supergiant shell (SGS) region in the northeast (Walter et al. 1998); a spatially resolved *Spitzer* case study of this SGS region is presented in Cannon et al. 2005. The elevated emission toward the southeast corner in the 160 μm image is caused by Galactic

[17] The National Radio Astronomy Observatory is a facility of the National Science Foundation operated under cooperative agreement by Associated Universities, Inc.

[18] The Astronomical Image Processing System (AIPS) has been developed by the NRAO.

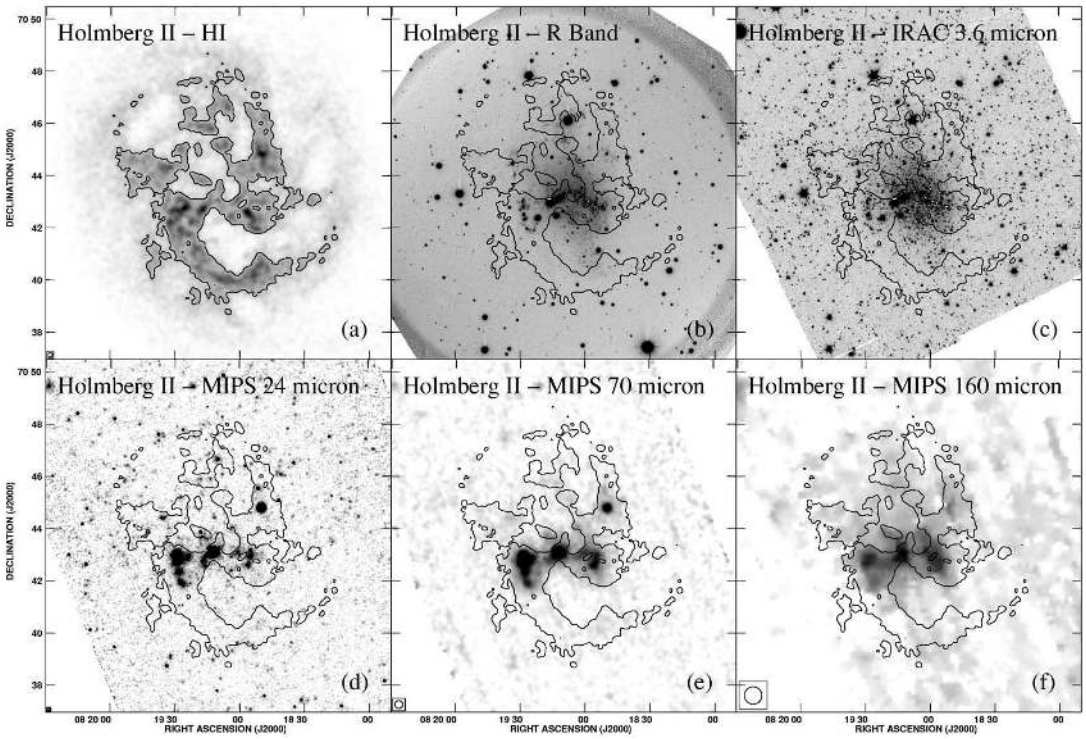

FIG. 2.—Holmberg II: (*a*) integrated THINGS H I map (contour shown at $N_{\rm H\,I} = 10^{21}$ cm^{-2} in all panels); (*b*) *R*-band image; (*c*) 3.6 μm image; (*d*, *e*, and *f*) 24, 70, and 160 μm images, respectively. The sizes of the H I and MIPS beams are given in the lower left corners of their respective panels.

cirrus emission (but this emission can be separated from the emission of IC 2574). Dust emission traced by the 70 μm emission is detected out to galactocentric radii of 7′ (∼7 kpc; see Fig. 8).

Holmberg II (*Fig. 2*).—The distribution of H I in Holmberg II is also characterized by the presence of numerous H I holes (Puche et al. 1992). As in the case of IC 2574, the changing morphologies in the individual MIPS bands and the corresponding changing spectral energy distributions stress the importance of local effects in characterizing the far-infrared emission (e.g., Cannon et al. 2005). The radial surface brightness profiles (Fig. 8) show that dust is detected out to at least 4′ (∼4 kpc).

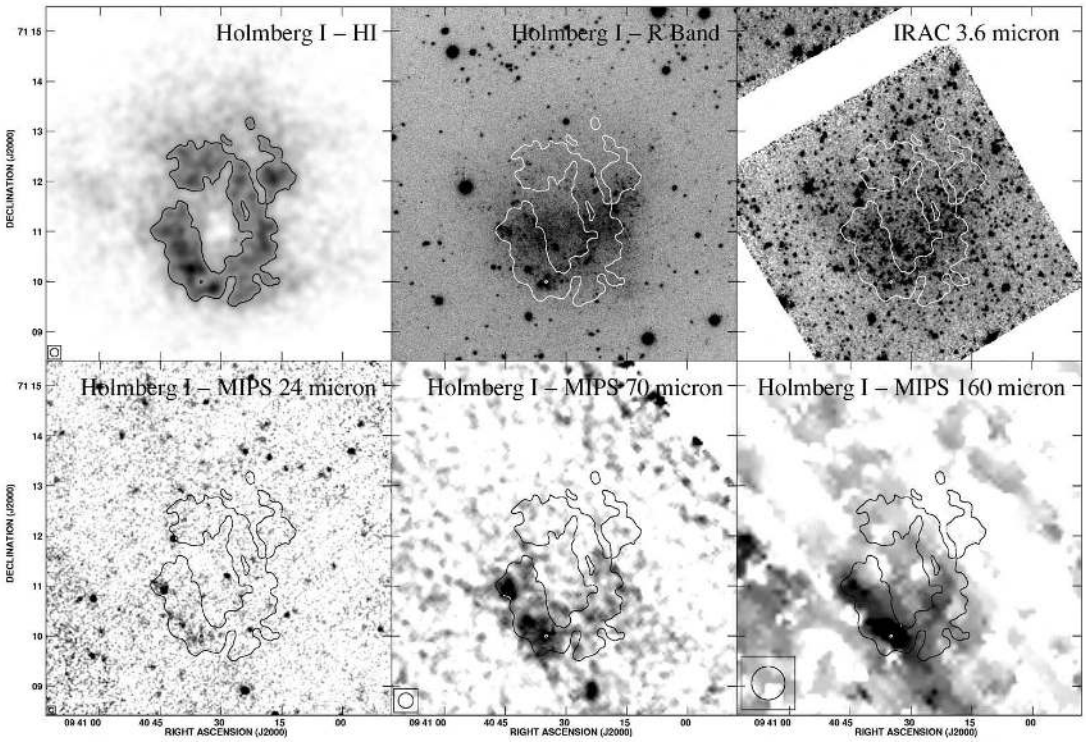

FIG. 3.—Holmberg I: (*a*) integrated THINGS H I map (contour shown at $N_{\rm H\,I} = 10^{21}$ cm^{-2} in all panels); (*b*) *R*-band image; (*c*) IRAC 3.6 μm image; (*d*, *e*, and *f*) 24, 70, and 160 μm images, respectively. The sizes of the H I and MIPS beams are given in the lower left corners of their respective panels.

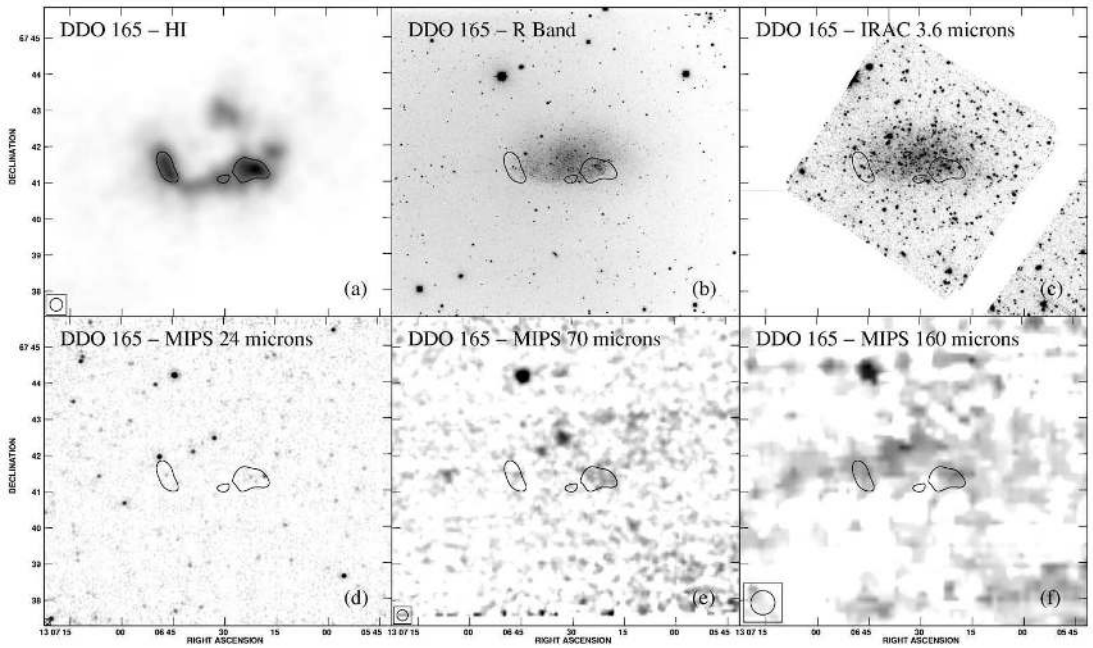

FIG. 4.—DDO 165: (*a*) integrated H I map at 21″ resolution (data from J. M. Cannon et al. 2007, in preparation; contour shown at $N_{\rm H\,I} = 10^{21}$ cm^{-2} in all panels); (*b*) *R*-band image; (*c*) IRAC 3.6 μm image; (*d*, *e*, and *f*) 24, 70, and 160 μm images, respectively. The sizes of the H I and MIPS beams are given in the lower left corners of their respective panels.

Holmberg I (*Fig. 3*).—The H I distribution in Holmberg I is characterized by one giant H I hole (Ott et al. 2001). The H I structure encompasses the optical emission and faint star formation is present on the rim toward the southeast (see also § 3.4). This is the region where faint emission is detected in all three MIPS bands. At 70 μm, there is also diffuse emission present toward the western H I rim (although this emission has a very low signal-to-noise ratio).

DDO 165 (*Fig. 4*).—DDO 165 shows extended emission in both the H I and the optical, but is not detected in the MIPS bands. The brightest emission seen in the 70 and 160 μm bands (toward the north) is a background galaxy (SDSS J130639.44+674456.4 at $z = 0.139$). There is some emission seen at 24 and 70 μm toward the center of DDO 165 (not coincident with the peak of the H I emission, and outside the main optical body of DDO 165)—future, higher sensitivity observations (MIPS and H I) are needed to see whether this emission is indeed physically related to DDO 165. Note that DDO 165 has one of the lowest star formation rates in our sample.

DDO 53 (*Fig. 5*).—The H I distribution shows two peaks, and the galaxy is detected in all three MIPS bands: The brightest

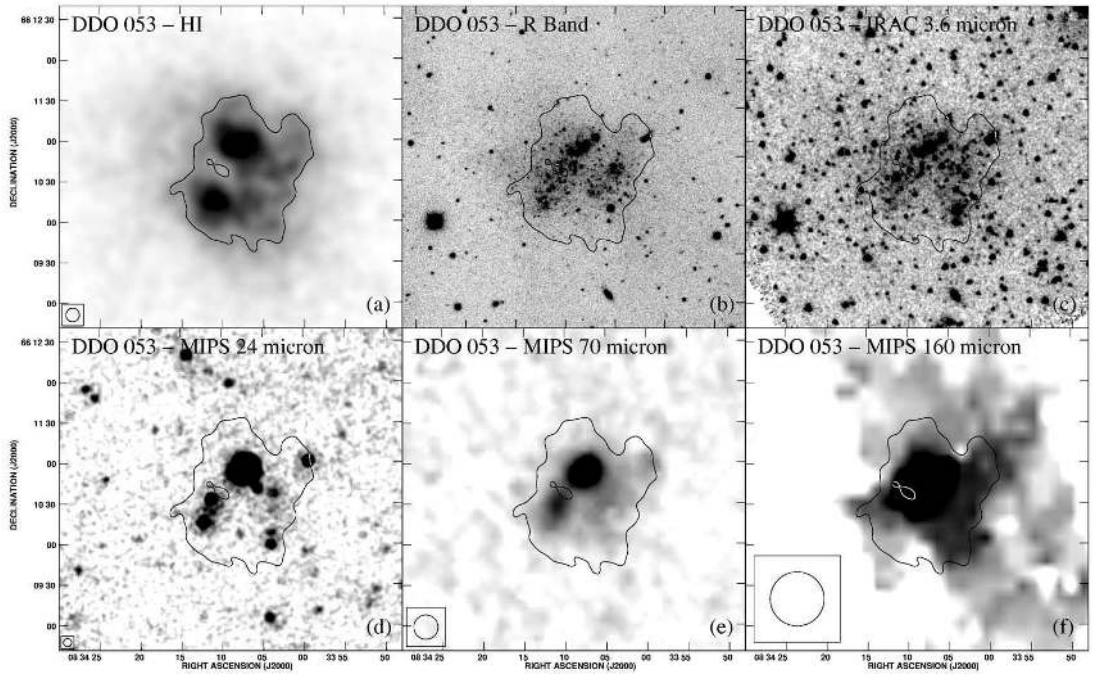

FIG. 5.—DDO 53: (*a*) integrated THINGS H I map (contour shown at $N_{\rm H\,I} = 10^{21}$ cm^{-2} in all panels); (*b*) *R*-band image; (*c*) IRAC 3.6 μm image; (*d*, *e*, and *f*) 24, 70, and 160 μm images, respectively. The sizes of the H I and MIPS beams are given in the lower left corners of their respective panels.

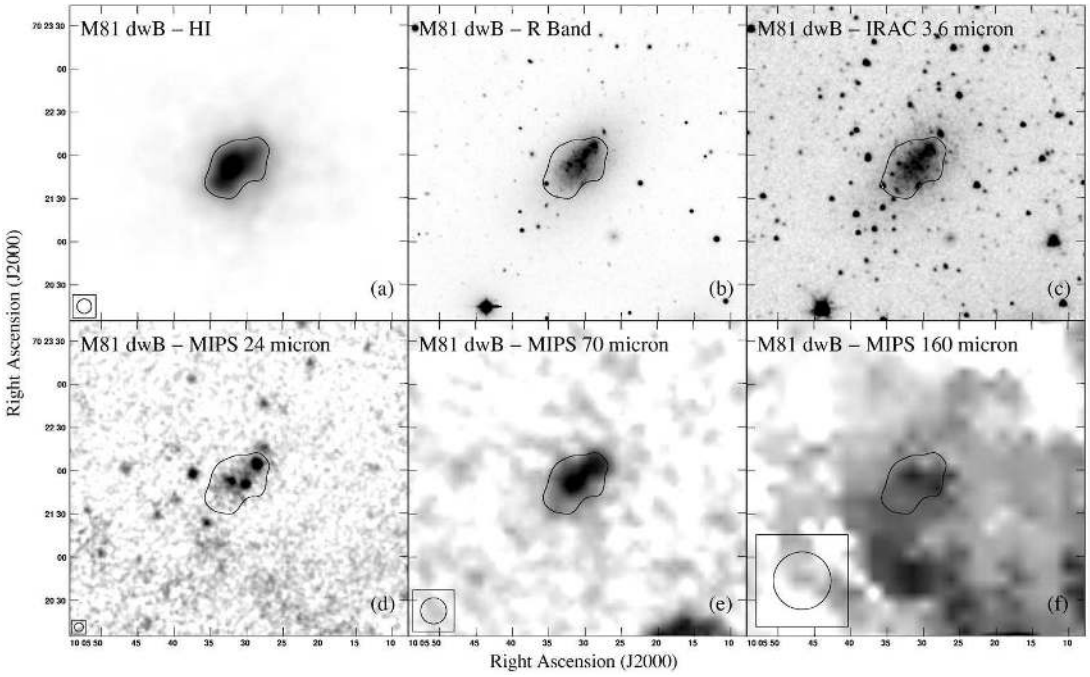

FIG. 6.—M81 dwB: (*a*) integrated THINGS H I map (contour shown at $N_{\rm H\,I} = 10^{21}$ cm^{-2} in all panels); (*b*) *R*-band image; (*c*) IRAC 3.6 μm image; (*d*, *e*, and *f*) 24, 70, and 160 μm images, respectively. The sizes of the H I and MIPS beams are given in the lower left corners of their respective panels.

emission seen at 24 μm is associated with the northern and southern H I peak; the northern region is also the strongest in the 70 μm image. The 160 μm data are noisy, but 160 μm emission is still present in the regions seen in the 70 μm image. The compact nature of DDO 53 is also evidenced by the radial surface brightness profiles shown in Fig. 8.

M81 dwB (*Fig. 6*).—M81 dwB is the galaxy with the lowest measured star formation rate in our sample. The galaxy shows a compact structure in H I and the MIPS bands (cf. Fig. 8). The detection at 160 μm is marginal (see Table 1) and is surrounded by elevated background emission present.

M81 dwA (*Fig. 7*).—M81 dwA is the faintest dwarf in our sample. Similar to Holmberg I, the H I distribution is characterized by one large H I shell which encompasses most of the optical galaxy. No ongoing star formation has been detected in M81 dwA (Miller & Hodge 1994); it is also a MIPS nondetection. This may be explained by the fact that H I column densities do not reach values higher than $N_{\rm H\,I} = 5 \times 10^{20}$ cm^{-2} in this galaxy

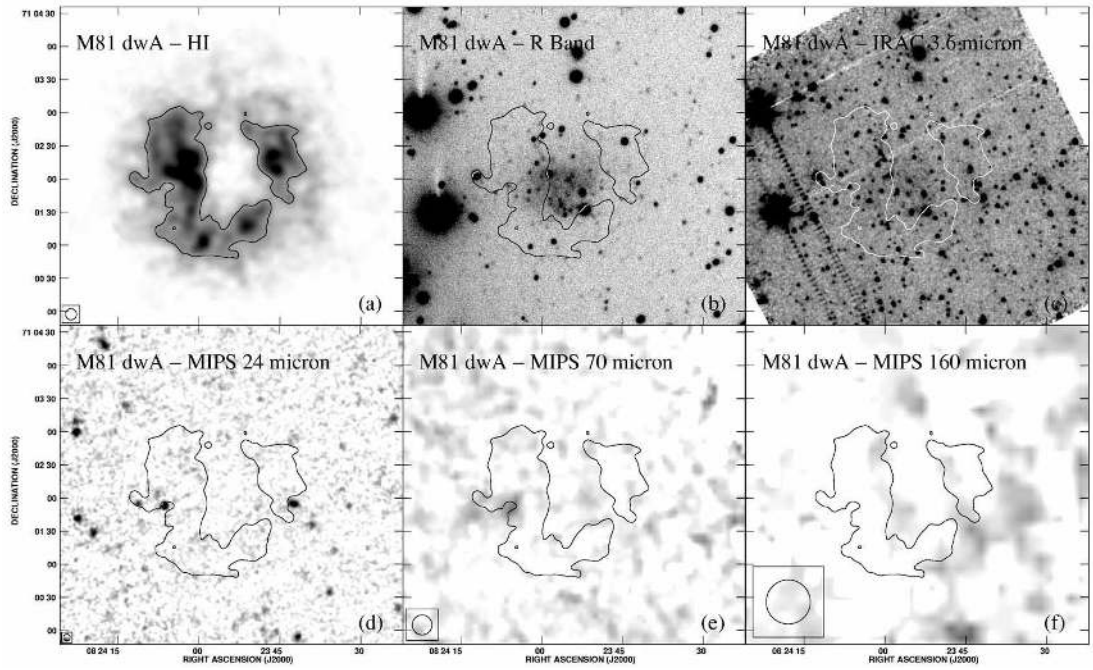

FIG. 7.—M81 dwA: (*a*) integrated THINGS H I map (contour shown at $N_{\rm H\,I} = 3 \times 10^{20}$ cm^{-2} in all panels); (*b*) *R*-band image; (*c*) IRAC 3.6 μm image; (*d*, *e*, and *f*) 24, 70, and 160 μm images, respectively. The sizes of the H I and MIPS beams are given in the lower left corners of their respective panels.

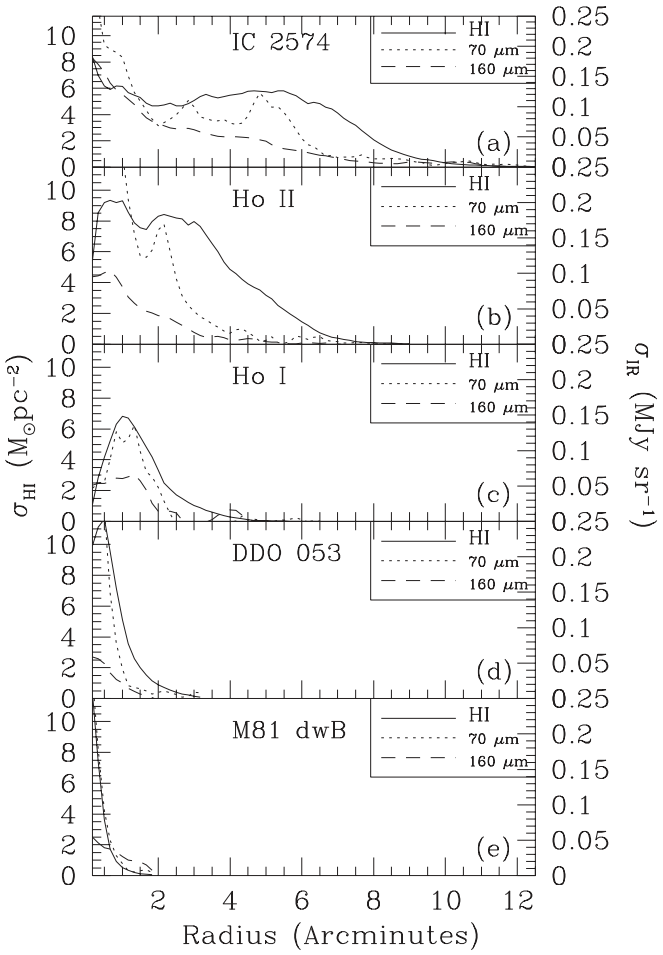

FIG. 8.—Comparison of the H I (*solid lines*), 70 μm (*short-dashed lines*), and 160 μm (*long-dashed lines*) radial profile of five M81 group dwarf irregular galaxies. The following deprojection parameters (position angle = P.A.; inclination = i) were used to create these profiles: IC 2574 [P.A. = +60°, i = 57°], Holmberg II [P.A. = −15°, i = 26°], Holmberg I [P.A. = 55°, i = 46°], DDO 53 [P.A. = −45°, i = 40°], and M81 dwB [P.A. = −60°, i = 46°].

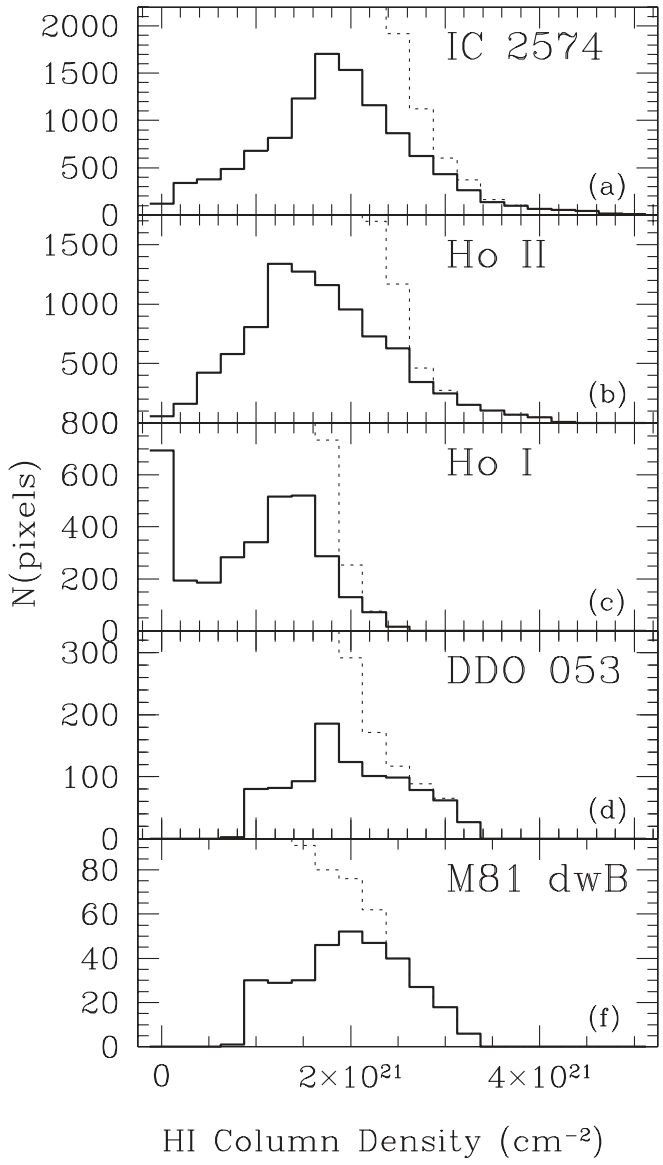

FIG. 9.—*Solid histogram:* Distribution of the 70 μm flux density above a threshold of 1.8 MJy sr^{-1} (~5 σ) as a function of H I column density. *Dashed histogram:* Total distribution of H I column densities.

(i.e., the H I column densities are below the canonical threshold for star formation).

3.1. H I *Threshold for Warm Dust*

From an inspection of the morphologies (Figs. 1–7) and radial profiles (Fig. 8) it is clear that the dust emission appears to be related to the distribution of the H I, at least to first order. To quantify this, we investigate whether there is a certain H I threshold above which most of the dust emission is present. In the following we use the 70 μm data as a tracer for the warm dust emission as they are (unlike the 24 μm data) not affected by the presence of contaminating point sources (stars and background objects) in the field. Furthermore, they have higher resolution and signal-to-noise ratio (S/N) than the 160 μm measurements. In Figure 9 we plot histograms of the distribution of the 70 μm flux density above a threshold of 1.8 MJy sr^{-1} (about the 5 σ level, i.e., encompassing most of the detected dust emission) as a function of H I column density for each galaxy (*solid histogram*). For each galaxy we also show the pixel-by-pixel distribution of all H I column densities (*dashed histogram*). From Figure 9 (and the previous discussion on the relative distribution of H I and 70 μm emission) we draw the following conclusions:

1. Most of the detected 70 μm emission is coincident with H I column densities of $N_{\rm H\,I} > 10^{21}$ cm^{-2} [with a peak around (1–2) × 10^{21} cm^{-2}]. In the case of Holmberg I, the peak in the first histogram bin at low surface densities is spurious and a result of the lower S/N in these data.

2. At high column densities (>2.5 × 10^{21} cm^{-2}), the solid (70 μm) and dashed (H I) histograms follow each other closely, implying that most of the high H I column density regions are associated with dust emission. In other words, there appear to be only few regions of high H I column densities that are *not* associated with warm dust emission.

3.2. *IRS Spectroscopy*

Selected regions in some of the galaxies in this sample have also been observed with the *Spitzer* IRS spectrograph (Houck et al. 2004a) as part of SINGS. In the following we will discuss IRS 5–14 μm, low-resolution spectra obtained for specific regions in the two most active galaxies in our sample, IC 2574 and Holmberg II (Fig. 10, both SFR ~ 0.1 $M_\odot$ yr^{-1}). The spectra have been extracted over a circular aperture of a diameter of ~14″ that was centered on the brightest region seen at 8 μm in

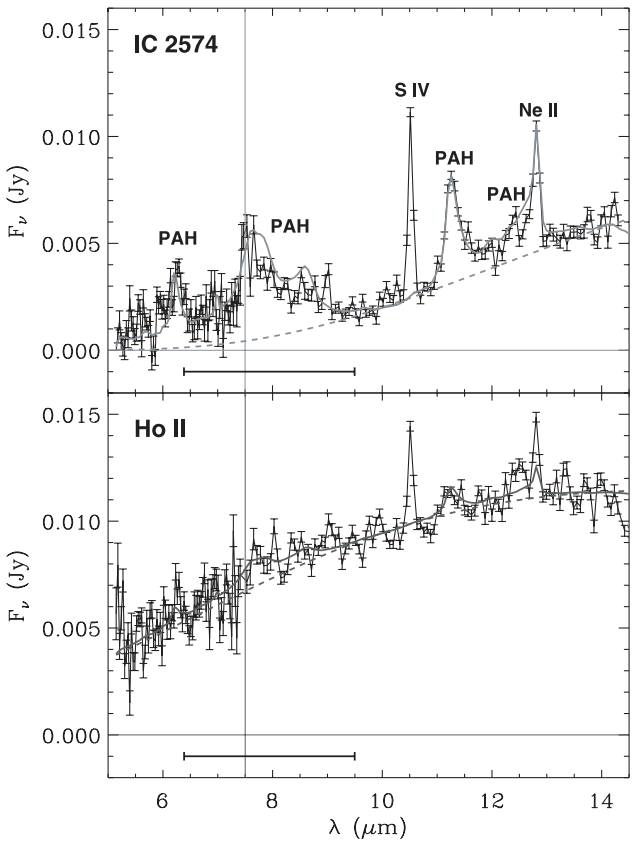

FIG. 10.— IRS spectra of IC 2574 (*top panel*) and Holmberg II (*bottom panel*). The vertical dashed line indicates the border of SL1 and SL2 modules of the IRS spectrograph. The thick gray lines represent the sum of our scaled PAH template (derived from SINGS observations of NGC 7552) and the underlying continuum (see text for details; *dashed curve*). The black horizontal line indicates the width (>10% response) of the IRAC band 4 filter.

both galaxies (see the caption of Table 2 for coordinates). For comparison, Table 3 also summarizes some of the IRAC flux densities obtained for the same apertures.

3.2.1. *IRS Spectrum of IC 2574*

The spectrum of IC 2574 (Fig. 10, *top panel*) clearly shows the broad emission features from polycyclic aromatic hydrocarbons (PAHs), which are typically found in mid-infrared spectra of massive star-forming galaxies (e.g., Telesco 1988; Lu et al. 2003; Smith et al. 2007). To derive a simple template for the aromatic/PAH features, we have taken the IRS spectrum of the SINGS galaxy NGC 7552 [$12 + \log(\mathrm{O/H}) \sim 8.5$; J. Moustakas et al. 2007, in preparation; SFR $\sim 7\,M_\odot\,\mathrm{yr}^{-1}$], which shows a typical spectrum with one of the highest S/Ns in the SINGS sample (Smith et al. 2007). From this spectrum we subtracted a 200 K blackbody spectrum that has been normalized to the pseudo-continuum at 10 and 13.5 μm. This PAH template was then scaled to fit the PAH feature at 11.3 μm in IC 2574 after a scaled blackbody spectrum of 200 K (*thick dashed line*) has been added (normalized in the same way as for NGC 7552; *thick gray line*). Although a blackbody is an unphysical representation of the dust continuum beneath the emission bands, this simple procedure allows us to compare the strength of the PAH bands in different sources in a consistent way. The relatively low S/N of the spectrum prevents a full spectral decomposition (e.g., as done by Smith et al. 2007).

It is interesting to note that this simple template fits the spectrum of IC 2574 quite well to first order. Even though the S/N ratio is low, the 7.7/11.3 μm PAH ratio in IC 2574 appears to be lower than in NGC 7552—band variations like that are known for many other galaxies (e.g., Draine & Li 2001; Vermeij et al. 2002, Cannon et al. 2006a; see detailed discussion in Smith et al. 2007). Engelbracht et al. (2005) showed that there appears to be a metallicity threshold of $12 + \log(\mathrm{O/H}) \sim 8.2$, below which PAH emission is not detected in galaxies.[19] The gas-phase metallicity of IC 2574 (Table 1) is slightly below their threshold—the fact that we do see PAH emission in IC 2574 is likely not due to metallicity variations within the galaxy (as no evidence of significant local metallicity variations has been found in dwarf galaxies; e.g., Kobulnicky & Skillman 1996, 1997), but rather due to other factors that influence the aromatic feature emission (e.g., radiation field, geometry, elemental composition of the ISM).

Two bright emission lines are present as well in the spectra of IC 2574: [Ne II] emission at 12.8 μm and [S IV] emission at 10.5 μm. The latter line is not present in the template spectrum of NGC 7552 and indicates the presence of massive stars—this line is usually found to be faint in massive galaxies (e.g., see discussion in Rigby & Rieke 2004), but bright in the highly ionized gas of blue compact dwarfs (e.g., Madden et al. 2006).

3.2.2. *IRS Spectrum of Holmberg II*

The IRS spectrum of Holmberg II (Fig. 10, *bottom panel*) is markedly different from that of IC 2574; the spectrum is dominated by continuum emission, and only very faint PAH features are present. The thick gray line again shows the comparison to our simple template: Here two blackbody curves (one at 300 K and one at 700 K, contributing equal flux density at 8.3 μm) were needed to adequately fit the continuum of Holmberg II (note again that these curves do not represent physically meaningful numbers but are only used to describe the shape of the continuum to first order; see also discussion in Smith et al. 2007); we then added a scaled version of our PAH template to this continuum emission (*thick gray line*). A comparison to this curve

[19] Note that the oxygen abundances used by Engelbracht et al. (2005) were based on a heterogeneous compilation of measurements from the literature, whereas the abundances in our study have been derived self-consistently, and placed on a common abundance scale (see J. Moustakas et al. 2007, in preparation for details).

TABLE 2
IRS VERSUS IRAC FLUX DENSITIES

Galaxy	$F(8\ \mu\mathrm{m})$ (mJy)	$F(6\ \mu\mathrm{m})$ (mJy)	$F(3.5\ \mu\mathrm{m})$ (mJy)	$F(8\ \mu\mathrm{m})_{\mathrm{IRS}}/F(8\ \mu\mathrm{m})_{\mathrm{IRAC}}$	$F(6\ \mu\mathrm{m})_{\mathrm{IRS}}/F(6\ \mu\mathrm{m})_{\mathrm{IRAC}}$
IC 2574[a]	3.10	1.39	0.73	0.89	0.95
Holmberg II[a]	8.53	5.75	2.02	0.93	0.81

[a] Central coordinates (J2000.0) and diameters D of circular apertures: IC 2574: R.A. = $10^{\mathrm{h}}28^{\mathrm{m}}48.3^{\mathrm{s}}$, decl. = $+68^\circ28'03''$, and $D = 13.67''$; Holmberg II: R.A. = $08^{\mathrm{h}}19^{\mathrm{m}}12.8^{\mathrm{s}}$, decl. = $+70^\circ43'08''$, and $D = 14.63''$.

TABLE 3
Dust and Gas Masses

Galaxy[a] (1)	M_{dust}[b] ($10^4\ M_\odot$) (2)	$M_{H\,I}$ ($10^8\ M_\odot$) (3)	$M_{H\,I}^{aptc}$ ($10^8\ M_\odot$) (4)	$M_{dust}/M_{H\,I}$ ($10^{-3}\ M_\odot$) (5)	$M_{dust}/M_{H\,I}^{apt}$ ($10^{-3}\ M_\odot$) (6)
IC 2574	72	14.75	2.8	0.49	2.6
Holmberg II	12	5.95	1.2	0.20	1.0
Holmberg I	6.8	1.40	0.4	0.48	1.7
DDO053	1.0	0.60	0.2	0.17	0.5

[a] See Table 1 for galaxy parameters.
[b] Dust mass derived using the SED models of Draine & Li (2006).
[c] H I mass in region where dust emission is present.

shows that, although the S/N is low, faint PAH features appear to be present at 6.2, 7.7, 11.3, and 12.7 μm—e.g., the 11.3 μm PAH feature is detected at 7 σ (total flux; peak: 4 σ). From this it is clear that the PAH-to-continuum ratio in Holmberg II is much lower than in the case of IC 2574 as discussed below. We note that the gas-phase metallicity of Holmberg II (Table 1) is lower than in IC 2574 by nearly a factor of 2 (below the threshold derived by Engelbracht et al., 2005). This result emphasizes the fact that the strength of the PAH features is not a simple linear function of metallicity (see also Smith et al. [2007], who find a wide range of PAH strengths [factor of $\sim$10] near the Engelbracht et al. threshold). As in the case of IC 2574, line emission from [Ne II] and [S IV] is detected in Holmberg II.

3.2.3. *PAH-to-Continuum Ratios*

Using our simple decomposition of the PAH features and the continuum emission, we can now constrain the PAH-to-continuum ratios for both galaxies. We do this for two bands: (1) the IRAC band 4 ("8 μm band"), encompassing the broad PAH features at 7.7 and 8.6 μm (see the horizontal line in Fig. 10 for the wavelength range covered by the 10% response of the IRAC band 4); and (2) the PAH band at 11.3 μm (here integrated within a mock square filter between 10.8 and 11.8 μm). We also calculate the PAH-to-total IR luminosity ratios for both regions below (but note that the method employed here is not directly comparable to the one used in Smith et al. 2007).

IC 2574.—From the IRS spectrum we derive a flux density of 2.7 mJy for the IRAC band 4 bandpass, which is in good agreement with the value derived from the actual IRAC band 4 measurement (3.0 mJy; see Table 3). The continuum contribution is 0.7 mJy and the contribution from the PAH features is 2.0 mJy; i.e., we derive a PAH-to-continuum ratio for this spectral region of $\sim$2.9. For the 11 μm feature we derive a ratio of 0.5 (continuum: 3.3 mJy, PAH: 1.7 mJy). Using our definitions for the 8 and 11 μm bandpasses and the total infrared (TIR) luminosities in this aperture (L_{TIR}, derived from the MIPS images and using the relation in Dale & Helou 2002), we get the following ratios: $L_{PAH,\,8\,\mu m}/L_{TIR} = 0.0089$ and $L_{PAH,\,11\,\mu m}/L_{TIR} = 0.0011$.

Holmberg II.—From the IRS spectrum we derive a flux density of 7.9 mJy for the IRAC band 4 bandpass, which is in good agreement with the value derived from the actual IRAC band 4 measurement (8.53 mJy; Table 3). The continuum contribution is 7.2 mJy, the contribution from PAHs is 0.7 mJy, leading to a PAH-to-continuum ratio of 0.1. For the 11 μm feature the ratio is even lower, 0.02 (continuum: 10.4 mJy, PAH: 0.2 mJy). The corresponding ratios compared to the total infrared luminosity in this aperture are $L_{PAH,\,8\,\mu m}/L_{TIR} = 0.0037$ and $L_{PAH,\,11\,\mu m}/L_{TIR} = 0.0002$. Given the faintness of the PAH features in Holmberg II, these values are uncertain (by $\sim$50%).

For comparison, we also derive the PAH-to-continuum ratios for our template galaxy NGC 7552 and get flux density ratios of 6.3 and 0.9 for the IRAC 4 and [10.8; 11.8] μm bandpasses, respectively. For the TIR luminosities we get the following ratios for NGC 7552: $L_{PAH,\,8\,\mu m}/L_{TIR} = 0.070$ and $L_{PAH,\,11\,\mu m}/L_{TIR} = 0.0077$; i.e., the ratio in IC 2574 is about a factor of 7 (Holmberg II: factor of >20) less than in our template galaxy (see Smith et al. 2007 for variations within the SINGS sample).

3.3. *Global Relations for the M81 Group Dwarfs*

In the following we compare the properties found for the M81 dwarf irregular galaxies to other galaxies in the SINGS sample (Kennicutt et al. 2003). To do so, we have divided the SINGS galaxies into four categories: the M81 group dwarf irregular galaxies of this study (11–13, *circles*), other dwarf galaxies (*open circles*), elliptical/S0s (*open squares*), and spiral galaxies (*crosses*). All MIPS flux densities for the SINGS galaxies are taken from Dale et al. (2006), and the gas-phase metallicities are taken from J. Moustakas et al. (2007, in preparation, based on the Pilyugin & Thuan 2005 strong-line abundance calibration).

As there apparently exists some correlation between the H I and the 70 μm emission (see discussion in the previous sections), we start by comparing the H I masses to the 70 μm specific luminosity[20] in Figure 11*a*. It is obvious that there is a large scatter between the two quantities (the dashed line indicates a linear relationship). If we plot the absolute blue magnitudes (M_B, taken from J. Moustakas et al. 2007, in preparation) as a function of the 70 μm specific luminosity instead (Fig. 11*b*), this relation gets tighter (*dashed line*). The larger scatter in the H I–70 μm relation is due to the fact that the dwarf irregular galaxies of our sample have more H I mass per blue magnitude compared to more massive spirals. This fact, i.e., that $M_{H\,I}/M_B$ increases for dwarf irregular galaxies was noted long before (e.g., Skillman 1996).

As a next step, we plot the star formation rates (SFRs) of individual galaxies as a function of the 70 μm specific luminosity (Fig. 12*a*). The SFRs were derived using $\mathrm{SFR} = L(\mathrm{H}\alpha_{corr})/1.26 \times 10^{41}\ \mathrm{ergs\ s^{-1}}\ (M_\odot\ \mathrm{yr^{-1}})$ (Kennicutt 1998; assuming solar metallicity and the Salpeter [1955]) initial mass function between 0.1 and 100 $M_\odot$). $L(\mathrm{H}\alpha_{corr})$ is the Hα luminosity corrected for extinction within the galaxy. Here we use the relation derived for SINGS galaxies by R. Kennicutt et al. (2007, in preparation) and D. Calzetti et al. (2007, in preparation): $F(\mathrm{H}\alpha)_{corr} = F(\mathrm{H}\alpha)_{obs} + 0.035 \times F'(24\ \mu m)$. $F(\mathrm{H}\alpha)_{obs}$ is the observed Hα flux (in ergs s^{-1} cm^{-2}, corrected for Galactic absorption and contribution from [N II]) taken from R. Kennicutt et al. (2007, in preparation) and Lee 2006; $F'(24\ \mu m)$ is defined as $F'(24\ \mu m) = 1.25 \times 10^{13}\ \mathrm{Hz} \times F(24\ \mu m)$ (Jy) [i.e., $F(24\ \mu m)$ multiplied by the observed frequency in Hz]. SFRs were only derived for those SINGS galaxies for which accurate Hα measurements are available. The tighter relation between $L(70\ \mu m)$ and SFR [as compared to the M_B-L (70 μm) relation discussed above], can (to first order) be explained by the fact that, typically, 70 μm is close to the peak of the far-IR emission and thus is a measure of the total bolometric luminosity, which is expected to scale with the SFR.

However, from Figure 12*a* it is also obvious that the galaxies do not follow a linear relation over all luminosities (as indicated by the dashed line). To exemplify this, the ratio of the 70 μm

[20] In the following we plot the specific luminosities (units of W Hz^{-1}). To derive the luminosities in a given MIPS band, this number needs to be multiplied by the effective bandwidth of the MIPS filter (in Hz). Note that some authors (e.g., Calzetti et al. 2005) define the luminosity as the specific luminosity times the observed frequency (in Hz).

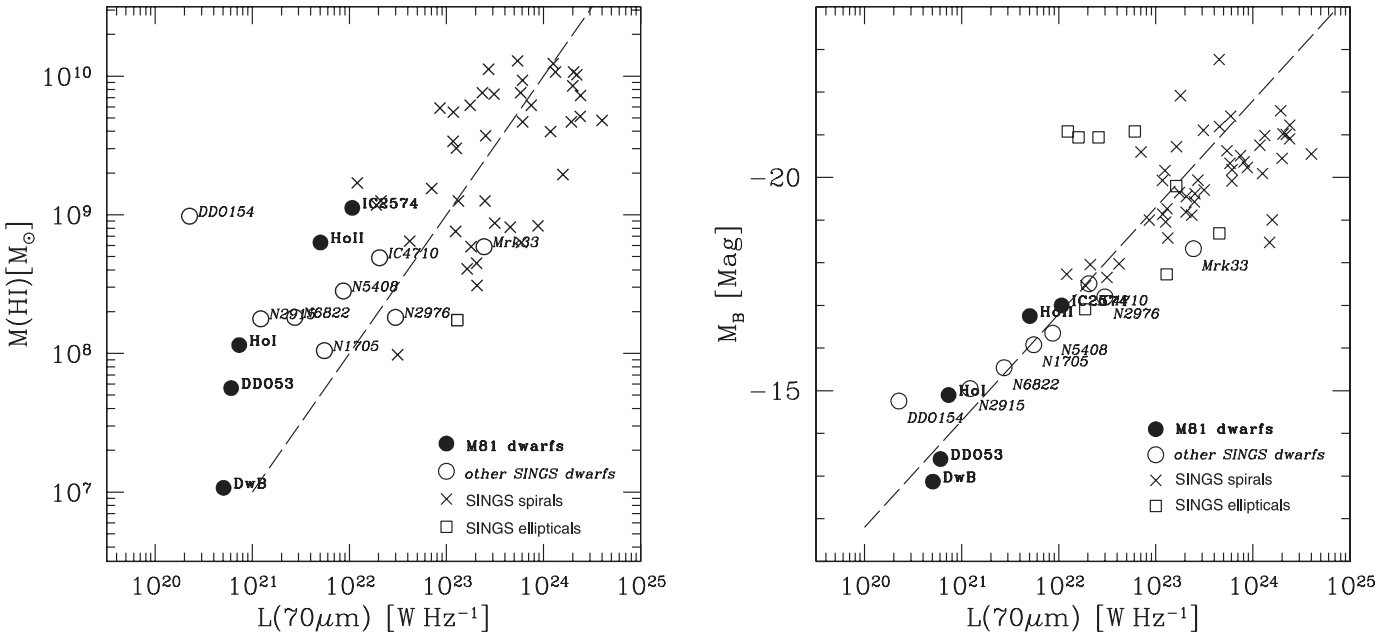

FIG. 11.—(*a*) H I mass as a function of 70 μm specific luminosity. (*b*) Blue magnitudes (M_B) as a function of 70 μm specific luminosity. The dashed line in both plots represents a linear relationship between the two variables.

specific luminosity and the SFR is plotted in Figure 12*b* as a function of the gas-phase oxygen abundance (taken from J. Moustakas et al. 2007, in preparation). If there was a linear relation between the 70 μm emission and the SFR, one would expect the symbols to lie near a horizontal line in this plot. However, the dwarfs, shown as circles, clearly occupy a lower $L_{70\ \mu\mathrm{m}}$/SFR space compared to the more massive galaxies. On average, the dwarf galaxies appear to be underluminous in 70 μm emission relative to their SFR by a factor of $\sim$2. A similar conclusion (dwarfs have lower $L_{\mathrm{IR}}/L_{\mathrm{H}\alpha}$) has been reached by Hunter et al. 1989, albeit for more luminous systems. This behavior may, to first order, be attributed to the fact that these objects have low metallicities and low dust contents (see discussion in § 3.5 and Draine et al. 2007). However, it is also clear that the scatter is large and that there is no simple relation between oxygen abundance and 70 μm luminosities per unit SF.

We now investigate how the global MIPS colors (here the 70/160 and 70/24 μm ratios) of the M81 groups dwarfs compare to the other SINGS galaxies. In Figure 13 we plot both ratios as a function of the oxygen abundance: Although the scatter is large, the dwarf galaxies have elevated 70/160 and 70/24 μm ratios compared to the spiral galaxies in SINGS. The elevated 70/160 μm ratios imply that the effective temperature of the dust in the dwarf irregular galaxies is on average higher than in more massive spirals. In this simplistic picture, the higher effective temperature

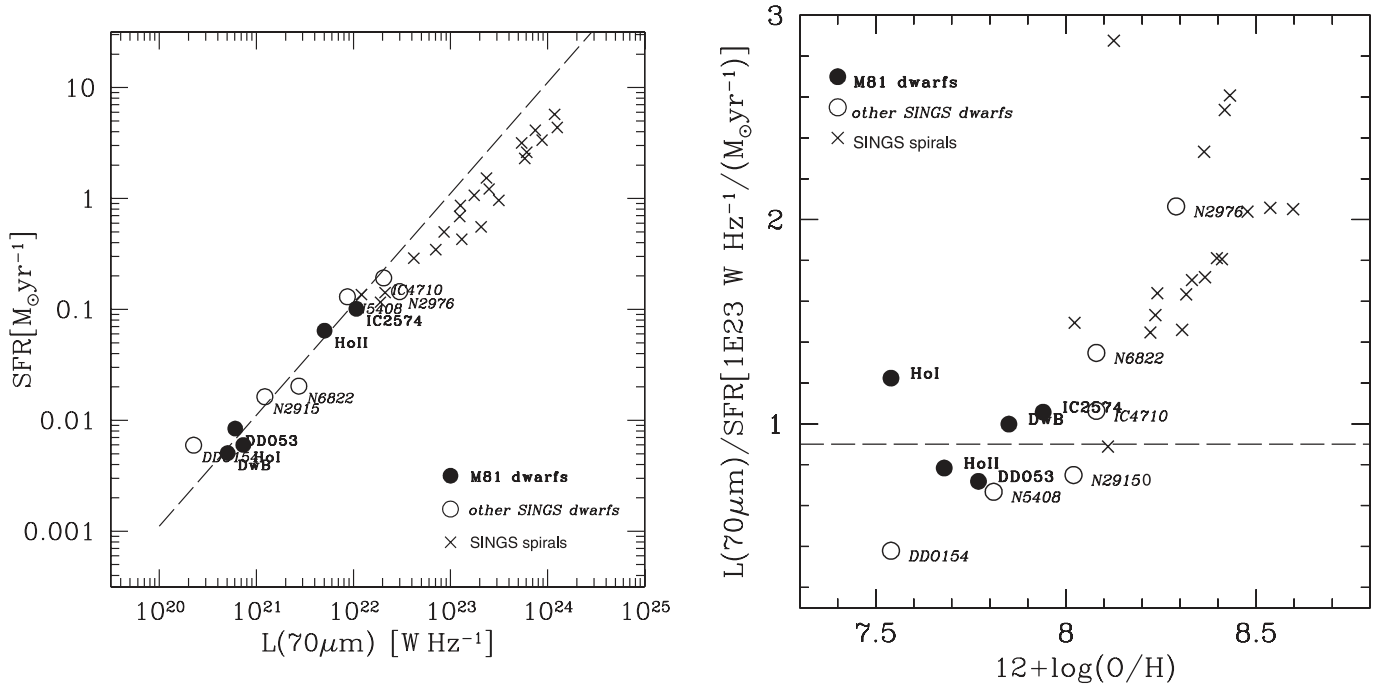

FIG. 12.—(*a*) SFR as a function of 70 μm specific luminosity. (*b*) Ratio of 70 μm specific luminosity and SFR as a function of metallicity. The dashed line in the left panel represents a linear relationship between the two variables (same relation as shown in the right panel).

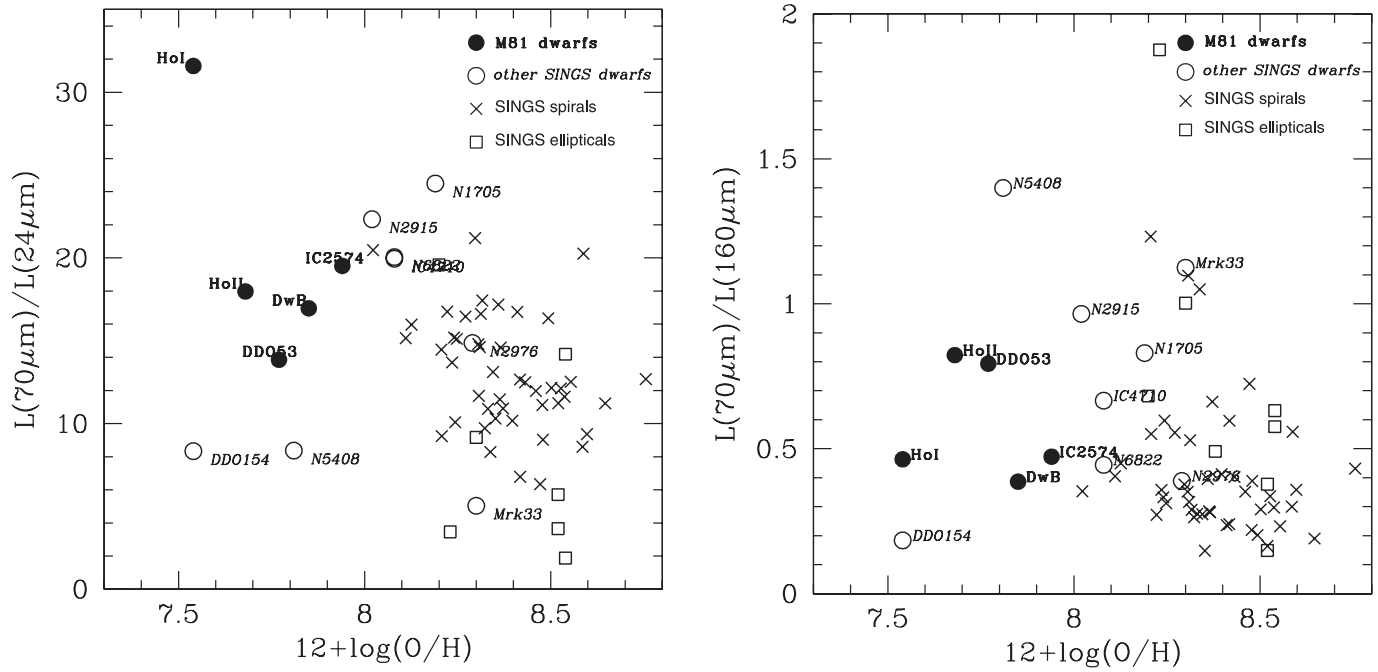

FIG. 13.—(*a*) 70–24 μm flux density ratio as a function of oxygen abundance. (*b*) 70–160 μm flux density ratio as a function of oxygen abundance.

results in a peak of the SED that is shifted toward the 70 μm wave band (cf. Hunter et al. 1989; Dale et al. 2005). In this context it is interesting to keep in mind that the $L_{70\ \mu m}$/SFR ratio in dwarfs is lower than in the spirals (see above). In other words, if the dust temperature in our sample dwarfs were the same as in the spirals, the $L_{70\ \mu m}$/SFR ratio would decrease even further.

The elevated 70/24 μm ratio in our sample dwarfs is more difficult to interpret as the origin of the 24 μm emission is not certain. According to the models by Draine & Li (2006), this emission is due to in part to single-photon heating, although in galaxies with strong 24 μm emission it is primarily due to warm grains in strong radiation fields. The 24 μm luminosity thus depends on the intensity of the radiation heating the dust (which depends on the density in the H II regions, the degree of clustering of O stars, as well as on the dust abundance). Future detailed modeling of the SEDs is needed to fully describe this behavior. We also note that our results do not necessarily hold for all classes of dwarf galaxies; i.e., extreme cases such as the metal-poor blue compact dwarf SBS 0335−052 have more extreme colors (very low 70/24 μm ratio; Houck et al. 2004b).

3.4. *Spatial Comparison to* Hα

The apparent strong correlation between the 70 μm luminosities and the SFR implies that the ongoing star formation is the main heating source for the warm dust. We now compare the spatial distribution of the Hα and the 70 μm emission: Figure 14

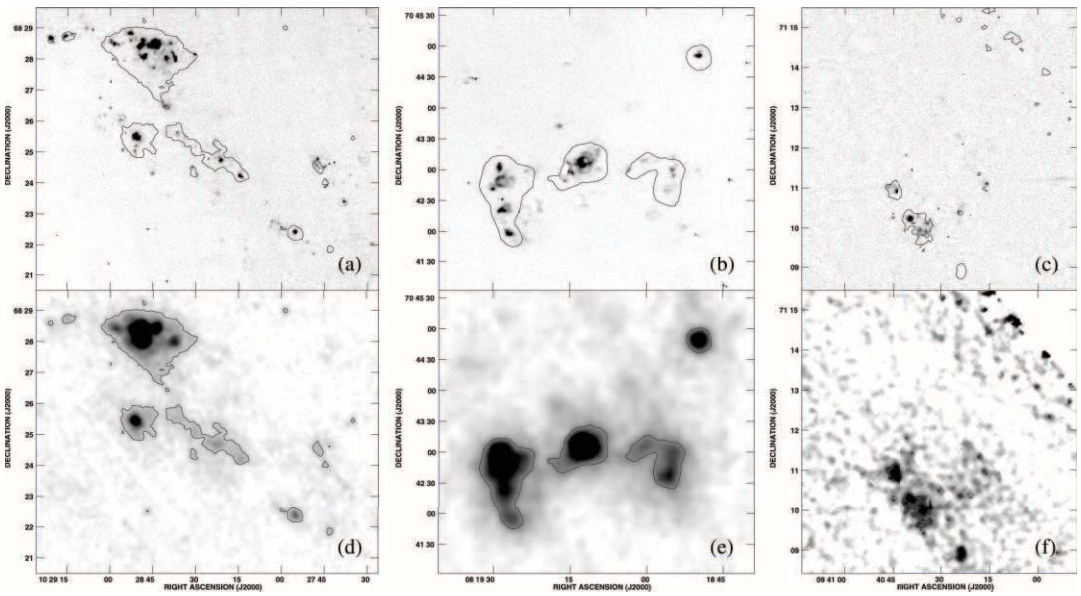

FIG. 14.—*Top:* Hα images for the three brightest dwarf galaxies in our sample: (*a*) IC 2574, (*b*) Holmberg II, and (*c*) Holmberg I. Contours indicate 70 μm surface brightness levels: (*a*) 1.8 MJy sr^{-1}, (*b*) 4 MJy sr^{-1}, and (*c*) 2.6 MJy sr^{-1}. *Bottom:* 70 μm maps of the three galaxies with the same contour overlaid (the emission seen toward the northwest of Holmberg I is noise).

(*top*) shows the Hα images for the three brightest Hα emitters in our sample (IC 2574, Holmberg II, and Holmberg I). The contour shown in the individual panels represents low-level 70 μm emission (shown in Fig. 14, *bottom*). From this we find a very good correlation between the locations of strong Hα and 70 μm emission. This has been found in other galaxies before (e.g., M51; Calzetti et al. 2005), but it is interesting to note that the same holds true even for faint dwarfs such as Holmberg I. We note that there is also diffuse dust emission present in our objects (e.g., Holmberg II and IC 2574) that is likely heated by the underlying stellar population or by UV photons that are leaking from the H II regions (see Cannon et al. [2006b] for a detailed discussion on the diffuse dust component in the Local Group galaxy NGC 6822; see also, e.g., Popescu et al. [2002], Popescu & Tuffs [2003], and Hinz et al. [2006]).

3.5. *Dust Masses*

We now discuss the dust masses of the M81 group dwarf irregular galaxies. As the dust mass derivations mostly rely on the longest wavelength MIPS bands (i.e., the 70 and 160 μm bands), and given the large error bars in the measurements of the dwarf galaxies discussed here (in particular in the 160 μm band, see Table 1), the dust masses presented in the following can only be considered to be order-of-magnitude estimates. Also, the observations are not sensitive to cold dust, which emits at wavelengths $\gg$160 μm (i.e., there may be more dust present that is not heated by star formation).

To estimate the dust masses we use a new model presented in Draine & Li (2006, based on the models presented in Li & Draine 2001 and 2002) that includes variable PAH abundances. In this model, radiation field strengths are varied via power-law distributions; PAH, silicate, and graphite grains are illuminated, and the resulting SEDs can be compared to the observations. Table 3 (col. [2]) summarizes the dust masses of the sample dwarf galaxies using their models (note that DDO 165 and M81 dwA were nondetections; the flux density measurements of M81 dwB are too uncertain to derive a meaningful dust mass): the dust masses span almost 2 orders of magnitude from $\sim(1.0\text{–}70)\times10^4\,M_\odot$. If we use the SED models by Dale et al. (2001) and Dale & Helou (2002), we get masses that are higher by a factor of $\sim$5. We attribute the difference to the fact that their models and dust mass correction factors were developed for normal galaxies and are therefore likely not appropriate for dwarfs.

With these dust masses we can now estimate the dust-to-gas ratios of the dwarf galaxies in our sample. In the following we define $M_{\rm gas} = M_{\rm H\,I}$ for the dwarfs, i.e., we do not take the possible (unknown) contribution of molecular gas into account (and we do not correct for the contribution of helium). Using our dust and H I masses (Table 3, col. [3]), we derive an average $M_{\rm dust}/M_{\rm H\,I}$ ratio of $\sim3\times10^{-4}$ (numbers for the individual galaxies are given in Table 3, col. [4]). These values do not appear to be a function of the measured metallicities (however, the spread in metallicies in the remaining sample is small). If we consider only the H I mass of the M81 group dwarfs in an aperture defined by the extent of the dust emission ($M_{\rm H\,I}^{\rm apt}$; Table 3, col. [5]), this ratio increases to an average of $M_{\rm dust}/M_{\rm H\,I}^{\rm apt}\sim1.5\times10^{-3}$ (Table 3, col. [6]). This is because, on average, about three-quarters of the extended H I mass has no associated bright dust emission (cf. Figs. 1–7).

Draine et al. (2007) present detailed dust mass estimates for all SINGS galaxies and derive a typical spread in dust-to-gas ratios for the more massive galaxies of $0.005 < M_{\rm dust}/M_{\rm gas} < 0.02$ (here including the contribution of molecular hydrogen). The value for the dwarfs is thus about an order of magnitude lower; it would decrease further if the dwarfs had a significant component of molecular hydrogen. The ratio for the dwarfs would increase, however, if they had an additional cold dust component (e.g., in the outskirts where the stellar radiation field is low; see also Draine et al. 2007) that cannot be traced with the available MIPS observations. For example, in the case of NGC 1569, Galliano et al. 2003 report a millimeter excess in the dust SED—this cold dust component could account for up to 70% of the total dust mass in this object. Such a cold reservoir may thus increase the total dust content by a factor of a few, but likely not by an order of magnitude. We thus conclude that the dust-to-gas ratio ($M_{\rm dust}/M_{\rm gas}$) in our sample dwarfs appears to be significantly lower than what is found in spiral galaxies (which cannot simply be explained by a linear scaling of this ratio with metallicity; see also the discussion in Draine et al. 2007).

4. SUMMARY

We present observations of warm dust and atomic gas in seven dwarf irregular galaxies in the M81 group using data from both SINGS and THINGS. Five of the seven targets have been detected with *Spitzer* out to 160 μm (the dwarfs with the lowest star formation rates, M81 dwA and DDO 165, are nondetections). As molecular gas in these systems has yet to be detected (the only likely exception is IC 2574; Leroy et al. 2005) the *Spitzer* observations give a first glimpse of the nature of the nonatomic ISM in these galaxies and provide important information to design follow-up observations of the molecular gas phase (e.g., to select regions of interest for pointed observations using millimeter telescopes).

We find that the warm dust emission as traced via the 70 μm observations is associated with high H I column densities ($N_{\rm H\,I}\sim1\times10^{21}$ cm^{-2}), close to the "canonical" star formation threshold found by previous studies (e.g., Skillman 1996; Walter & Brinks 1999; Schaye 2004). Most regions with H I column densities of $N_{\rm H\,I} > 2.5\times10^{21}$ cm^{-2} have dust emission associated with them. For the brightest regions at 70 μm there is a good correlation with the location of H II regions, indicating that active star formation is needed to heat up the dust locally. However, in some cases, there is diffuse dust emission present at larger radii that does not appear to coincide with compact H II regions. This diffuse emission is likely due to the reprocessing of nonionizing photons in the ISM or the escape of radiation from the star formation regions (see also Cannon et al. 2006b).

IRS spectroscopy in the brightest regions in IC 2574 and Holmberg II (which have comparable star formation rates) reveal distinctly different spectral shapes: Whereas PAH features are clearly detected in the spectrum of IC 2574, those features are weaker in Holmberg II (which has lower metallicity) by an order of magnitude. This emphasizes that the strength of PAH features is not a simple linear function of metallicity (see also Smith et al. 2007). The PAH-to-TIR continuum ratio in IC 2574 is a factor of $\sim$7 less than what is found in a typical SINGS spiral (a factor of >20 in the case of Holmberg II).

While the H I masses are well constrained, it is difficult to constrain the dust masses with a high degree of certainty. We estimate dust masses of $\sim10^4$–$10^6\,M_\odot$ for individual targets, resulting in an average dust-to-gas ratio ($M_{\rm dust}/M_{\rm H\,I}$) of $\sim3\times10^{-4}$ (1.5×10^{-3} if only the H I that is associated with dust emission is considered). This can be compared to the range in values derived for the SINGS galaxies by Draine et al. (2007) of $0.005 < M_{\rm dust}/M_{\rm gas} < 0.02$. Thus, the average dust-to-gas ratio in the dwarfs is lower by about an order of magnitude as compared to more massive spirals (a finding that cannot simply be explained by a linear scaling with metallicity; see also Draine et al. 2007). Future sensitive observations at longer (submillimeter) wavelengths

are critical to constrain the possible presence of a colder dust component in the galaxies (not heated by the stellar population) that may be missed by the MIPS observations.

We also find that the dwarf galaxies in our sample are underluminous at 70 μm for a given SFR by about a factor of $\sim$2 compared to the more massive and metal-rich galaxies in SINGS. However, interestingly, the average 70/160 μm ratio in the dwarfs is higher (factor of $\sim$2) than in the spiral galaxies. In a simplistic picture, this can be attributed to higher effective dust temperatures in the dwarf galaxies (which shifts the peak of the warm dust SED toward 70 mm; cf. Dale et al. 2005). Similar conclusions on the dust temperature have been derived by other authors studying more luminous dwarf systems (Hunter et al. 1989; Dale et al. 2005; Engelbracht et al. 2005; Cannon et al. 2005; 2006a, 2006b) and have been explained in the context of stronger radiation fields in the dwarfs. It is interesting to note that, if the dwarf galaxies had the same temperature as the more massive spirals, the 70 μm luminosity for a given SFR would decrease further (relative to the spirals). Overall, there is a better correlation between the SFR (or optical magnitudes) and the 70 μm luminosity than between the H I mass and L(70 μm). This provides additional evidence that the far-IR emission in the sample dwarf galaxies is powered by ongoing star formation and does not strongly depend on the total H I mass of the galaxy host.

Some of the data presented here are part of the *Spitzer Space Telescope* Legacy Science Program The *Spitzer* Nearby Galaxies Survey (SINGS), which was made possible by NASA through contract 1224769 issued by JPL/Caltech under NASA contract 1407. This work was also supported in part by NSF grant AST 04-06883.

REFERENCES

Asplund, M., Grevesse, N., & Sauval, A. J. 2005, in ASP Conf. Ser. 336, Cosmic Abundances as Records of Stellar Evolution and Nucleosynthesis, ed. T. G. Barnes III & F. N. Bash (San Francisco: ASP), 25
Barone, L. T., Heithausen, A., Hüttemeister, S., Fritz, T., & Klein, U. 2000, MNRAS, 317, 649
Bendo, G. J., et al. 2006, ApJ, 652, 283
Calzetti, D., et al. 2005, ApJ, 633, 871
Cannon, J. M., et al. 2005, ApJ, 630, L37
———. 2006a, ApJ, 647, 293
———. 2006b, ApJ, 652, 1170
Dale, D. A., & Helou, G. 2002, ApJ, 576, 159
Dale, D. A., Helou, G., Contursi, A., Silbermann, N. A., & Kolhatkar, S. 2001, ApJ, 549, 215
Dale, D. A., et al. 2005, ApJ, 633, 857
———. 2006, ApJ, 646, 161
de Vries, H. W., Thaddeus, P., & Heithausen, A. 1987, ApJ, 319, 723
Draine, B. T., & Li, A. 2001, ApJ, 551, 807
———. 2006, ApJ, 657, 810
Draine, B., et al. 2007, ApJ, in press (astro-ph/0703213)
Engelbracht, C. W., Gordon, K. D., Rieke, G. H., Werner, M. W., Dale, D. A., & Latter, W. B. 2005, ApJ, 628, L29
Engelbracht, C. W., et al. 2004, ApJS, 154, 248
Gallagher, J. S., Hunter, D. A., Gillett, F. C., & Rice, W. L. 1991, ApJ, 371, 142
Galliano, F., Madden, S. C., Jones, A. P., Wilson, C. D., Bernard, J.-P., & Le Peintre, F. 2003, A&A, 407, 159
Gordon, K. D., et al. 2005, PASP, 117, 503
Hinz, J. L., Misselt, K., Rieke, M. J., Rieke, G. H., Smith, P. S., Blaylock, M., & Gordon, K. D. 2006, ApJ, 651, 874
Houck, J. R., et al. 2004a, ApJS, 154, 18
———. 2004b, ApJS, 154, 211
Hunter, D. A., Gallagher, J. S., Rice, W. L., & Gillett, F. C. 1989, ApJ, 336, 152
Hunter, D. A., et al. 2001, ApJ, 553, 121
Jackson, D. C., Cannon, J. M., Skillman, E. D., Lee, H., Gehrz, R. D., Woodward, C. E., & Polomski, E. 2006, ApJ, 646, 192
Jörsäter, S., & van Moorsel, G. A. 1995, AJ, 110, 2037
Karachentsev, I. D., et al. 2002, A&A, 383, 125
———. 2003, A&A, 398, 479
Kennicutt, R. C. 1998, ARA&A, 36, 189
Kennicutt, R. C., et al. 2003, PASP, 115, 928
Kobulnicky, H. A., & Skillman, E. D. 1996, ApJ, 471, 211
———. 1997, ApJ, 489, 636
Lee, J. C. 2006, Ph.D. thesis, Univ. Arizona
Leroy, A., Bolatto, A. D., Simon, J. D., & Blitz, L. 2005, ApJ, 625, 763
Li, A., & Draine, B. T. 2001, ApJ, 554, 778
———. 2002, ApJ, 576, 762
Lu, N., et al. 2003, ApJ, 588, 199
Madden, S. C., Galliano, F., Jones, A. P., & Sauvage, M. 2006, A&A, 446, 877
Melisse, J. P. M., & Israel, F. P. 1994a, A&A, 285, 51
———. 1994b, A&AS, 103, 391
Miller, B. W., & Hodge, P. 1994, ApJ, 427, 656
O'Halloran, B., Satyapal, S., & Dudik, R. P. 2006, ApJ, 641, 795
Ott, J., Walter, F., Brinks, E., Van Dyk, S. D., Dirsch, B., & Klein, U. 2001, AJ, 122, 3070
Pilyugin, L. S., & Thuan, T. X. 2005, ApJ, 631, 231
Popescu, C. C., & Tuffs, R. J. 2003, A&A, 410, L21
Popescu, C. C., Tuffs, R. J., Völk, H. J., Pierini, D., & Madore, B. F. 2002, ApJ, 567, 221
Puche, D., Westpfahl, D., Brinks, E., & Roy, J.-R. 1992, AJ, 103, 1841
Rigby, J. R., & Rieke, G. H. 2004, ApJ, 606, 237
Rosenberg, J. L., Ashby, M. L. N., Salzer, J. J., & Huang, J.-S. 2006, ApJ, 636, 742
Salpeter, E. E. 1955, ApJ, 121, 161
Schaye, J. 2004, ApJ, 609, 667
Skillman, E. D. 1996, in ASP Conf. Ser. 106: The Minnesota Lectures on Extragalactic Neutral Hydrogen, ed. E. D. Skillman (San Francisco: ASP), 208
Smith, J. D. T., et al. 2007, ApJ, 656, 770
Taylor, C. L., Kobulnicky, H. A., & Skillman, E. D. 1998, AJ, 116, 2746
Telesco, C. M. 1988, ARA&A, 26, 343
Vermeij, R., Peeters, E., Tielens, A. G. G. M., & van der Hulst, J. M. 2002, A&A, 382, 1042
Walter, F., & Brinks, E. 1999, AJ, 118, 273
Walter, F., Brinks, E., de Blok, W. J. G., Thornley, M. D., & Kennicutt, R. C. 2005, in ASP Conf. Ser. 331, Extra-Planar Gas, ed. R. Braun (San Francisco: ASP), 269
Walter, F., Walter, F., Kerp, J., Duric, N., Brinks, E., & Klein, U. 1998, ApJ, 502, L143
Wu, Y., Charmandaris, V., Hao, L., Brandl, B. R., Bernard-Salas, J., Spoon, H. W. W., & Houck, J. R. 2006, ApJ, 639, 157